

## Observation of higher-order exceptional points in a non-local acoustic metagrating

Xinsheng Fang<sup>1</sup>, Nikhil J R K Gerard<sup>2</sup>, Zhiling Zhou<sup>1</sup>, Hua Ding<sup>1</sup>, Nengyin Wang<sup>1</sup>, Bin Jia<sup>1</sup>, Yuanchen Deng<sup>2</sup>, Xu Wang <sup>1✉</sup>, Yun Jing <sup>2✉</sup> & Yong Li <sup>1✉</sup>

Higher-order exceptional points have attracted increased attention in recent years due to their enhanced sensitivity and distinct topological features. Here, we show that non-local acoustic metagratings enabling precise and simultaneous control over their multiple orders of diffraction can serve as a robust platform for investigating higher-order exceptional points in free space. The proposed metagratings, not only could advance the fundamental research of arbitrary order exceptional points, but could also empower unconventional free-space wave manipulation for applications related to sensing and extremely asymmetrical wave control.

<sup>1</sup>Institute of Acoustics, School of Physics Science and Engineering, Tongji University, Shanghai 200092, China. <sup>2</sup>Graduate Program in Acoustics, Penn State University, University Park, PA 16802, USA. ✉email: [xuwang@tongji.edu.cn](mailto:xuwang@tongji.edu.cn); [jing.yun@psu.edu](mailto:jing.yun@psu.edu); [yongli@tongji.edu.cn](mailto:yongli@tongji.edu.cn)

Exceptional points (EPs) are singularities in parameter space, uniquely supported by non-Hermitian systems<sup>1–7</sup>. EPs for classical waves have been realized by employing gain and/or loss, and unconventional wave behaviors have been demonstrated when the eigenvalues and eigenvectors of the system's Hamiltonian or scattering matrix (S-matrix) simultaneously coalesce. Pivoted on the concept of EPs, new mechanisms for controlling light<sup>8–12</sup> and sound<sup>13–16</sup> have been identified. Examples include but are not limited to unidirectional wave propagation<sup>9,11,12,15</sup>, coherent perfect absorption<sup>16</sup>, and phonon lasing<sup>17</sup>. Early research in non-Hermitian wave physics showed that 2nd-order EPs can be realized by using two coupled cavities or waveguides, and such low-order EPs can be leveraged for sensing applications<sup>18–20</sup>. Subsequent studies, however, emerged to show that a far greater sensitivity can be realized at higher-order EPs<sup>6</sup>. These higher-order EPs were made possible by increasing the number of cavities or waveguides in the system<sup>6,14,21,22</sup>. The major downside of this scheme, however, is that the waves are confined in closed systems and hence limited to 0-D or 1-D wave propagation. EPs for open systems permitting wave propagation in higher-dimensions, on the other hand, would entail richer physics and offer a greater variety of wave functionalities.

Driven by these prospects, more recent studies have drawn inspiration from the progress in 2D wave functional materials<sup>23–28</sup> and shown that lossy acoustic metasurfaces<sup>15,29–33</sup> could serve as a fertile platform for engineering EPs. In particular, it was illustrated that a second-order EP derived from a  $2 \times 2$  scattering matrix, which portrays a 2-channel metasurface, could give rise to extremely asymmetrical retro-reflection<sup>30</sup>. Extending this concept to higher-order EPs, however, is not trivial, since conventional metasurfaces do not offer precise and simultaneous control over the multiple propagating orders existing in the corresponding higher-order scattering matrices, which is instrumental for achieving higher-order EPs. This hurdle can be attributed to the fact that traditional metasurfaces treat each subunit separately without considering their non-local interaction, and as a result the diffraction efficiency is fundamentally limited.

This paper reports on the experimental observation of a higher-order EP in an open acoustic system, and illustrates that non-local metagrating<sup>34–37</sup> is the key enabler for this observation. We start by establishing a mathematical framework to construct an S-matrix that can give rise to arbitrary order EPs. The metagratings that are then proposed comprise lossy and non-lossy sub-units, where the former represents loss in a passive Parity-Time ( $\mathcal{PT}$ ) symmetric medium<sup>15</sup>. Our non-local metagratings can be conveniently tuned to tailor the S-matrix, offering a robust approach for engineering EPs of arbitrary orders. This is enabled by harnessing the non-local response of the constituent sub-units via evanescent wave fields, thereby offering the ability to efficiently mold the energy flow to multiple channels of reflection.

## Results

### Generalized higher-order degeneracy in a scattering system.

Without loss of generality, a square matrix,  $A$ , of arbitrary order,  $N$ , has its eigenvalues and eigenvectors coalesce simultaneously only when it is a *similarity matrix* of the Jordan-block canonical form,  $J$ , which can be expressed as:

$$A^{(N)} \sim J^{(N)}(E_0) = \begin{pmatrix} E_0 & 1 & & & & \\ & E_0 & 1 & & & \\ & & \ddots & \ddots & & \\ & & & E_0 & 1 & \\ & & & & E_0 & \\ & & & & & E_0 \end{pmatrix}, \quad (1)$$

where  $\sim$  denotes similarity and  $E_0$  is the degenerate eigenvalue. Here, accessing the EPs in higher-order S-matrices resorts to a scattering system (i.e., a grating) that offers complete control over the multiple modes of diffraction.

As per the classical diffraction theory, the relationship between the incoming wave and an  $n$ -th order diffracted wave reads  $k_0(\sin \theta_r - \sin \theta_i) = nG$ , which is also known as the generalized law of reflection. Here,  $k_0$  is the wavenumber in free space and  $\theta_i$  and  $\theta_r$  are the angles of incidence and reflection, respectively.  $G = 2\pi/D$  is the reciprocal lattice vector, where  $D$  is the grating period that can be tailored to enable different orders of diffraction. Here we assume the operating frequency is 3430 Hz. In the case of the third-order reflected system, for example, we require the existence of three propagating channels (Fig. 1), left  $45^\circ$ , normal  $0^\circ$ , and right  $-45^\circ$ , respectively. Then  $\sin \theta_i, \sin \theta_r \in (-\sqrt{2}/2, 0, \sqrt{2}/2)$ . Substituting these into the generalized law of reflection, then  $D$  must be  $\sqrt{2}$  times the wavelength,  $\lambda$ , and would result in a  $G = (\sqrt{2}k_0)/2$ . The response of the resulting system can be then described as  $\{p_r^R, p_r^N, p_r^L\}^T = S\{p_i^L, p_i^N, p_i^R\}^T$ , where the vector on the left denotes the output sound field (reflection) while that on the right denotes the input (incidence). Here,  $p$  is the complex pressure amplitude, whose superscript indicates the left (L), normal (N) and right (R) channels of the grating, and the subscript refers to the reflection ( $r$ ) or incidence ( $i$ ). The S-matrix that connects these two vectors can be written as:

$$S = \begin{pmatrix} r_0^L & r_{+1}^N & r_{+2}^R \\ r_{-1}^L & r_0^N & r_{+1}^R \\ r_{-2}^L & r_{-1}^N & r_0^R \end{pmatrix}, \quad (2)$$

where the individual elements denote the reflection coefficient of each mode. The superscripts indicate the directions of incidence and the subscripts represent the orders of reflection. The non-clinodiagonal terms correspond to the specular ( $r_0^L, r_0^R$ ) and anomalous reflection ( $r_{-1}^L, r_{-1}^N, r_{+1}^N, r_{+1}^R$ ) cases, where in both cases the wave is reflected to a port different from that of the incident one. The clinodiagonal terms ( $r_{-2}^L, r_0^N, r_{+2}^R$ ) of the matrix

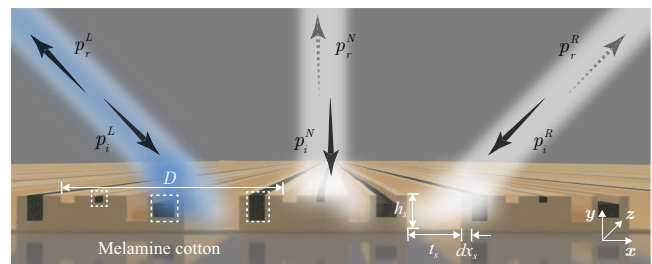


**Fig. 1 Schematic diagram of a non-local and non-Hermitian acoustic metagrating at the higher-order exceptional point.** This metagrating is composed of six surface-etched grooves in a period ( $D$ ). The global response of the metagrating to the external excitation can be engineered by tuning the groove depth ( $h_s$ ), width ( $t_s$ ), and the spacing ( $dx_s$ ), where  $s$  is the index of groove in a period ( $s = 1, 2, \dots, 6$ ). The variation of  $dx_s$  can be used to tune the non-local interaction between grooves. White and blue rays show the channels with strong and eliminated retro-reflection, respectively. The propagating waves are represented by black arrows, while the suppressed waves are indicated by gray dashed arrows.  $p$  is the complex pressure amplitude, whose superscript indicates the left (L), normal (N) and right (R) channels of the grating, and the subscript refers to the reflection ( $r$ ) and incidence ( $i$ ). In each period, three grooves are filled with sound-absorbing materials (melamine cotton) to introduce loss, as marked by white dashed rectangles.

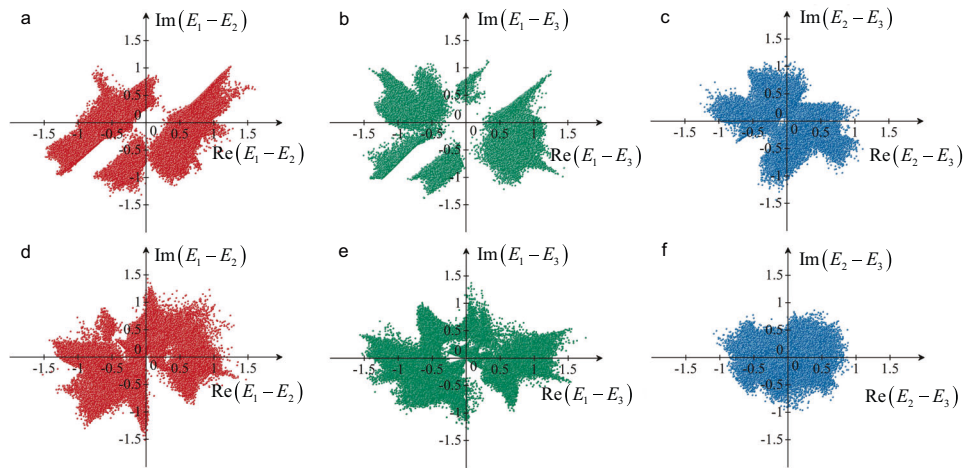


**Fig. 2** Difference between eigenvalues ( $E_1, E_2, E_3$ ) of gradient index metasurfaces and non-local metagratings. The x-axis represents the real part of the difference while the y-axis shows the imaginary part. The dots represent samples with randomly assigned imaginary parts of sound speed for gradient index metasurfaces (**a-c**) and samples with randomly assigned real and imaginary parts of sound speed for non-local metagratings (**d-f**).

denote retro-reflection, where the wave goes back in the same direction from where it is incident.

Here, we focus on an extreme scenario where  $r_{+1}^L, r_0^N, r_0^R, r_{+1}^R, r_{+1}^R$ , and  $r_{+2}^R$  all vanish,  $r_{-2}^L$  is as large as possible, while  $r_{-1}^L$  and  $r_{-1}^N$  approach zero (they cannot be exactly zero, otherwise the system will just yield a second-order EP). With the target S-matrix,  $(0, 0, 0; \sim 10^{-2}, 0, 0; 1, \sim 10^{-2}, 0)$ , our design results in an acoustic mirror that strongly retro-reflects the wave that is incident from one direction, but near completely absorbs those incident from the other two directions, as shown in Fig. 1. Note that, we choose to demonstrate the third-order EP with the most asymmetrical wave behavior, while other types of third-order EPs also exist in the three-channel scattering system. See another example at a different third-order EP in Supplementary Note 1.

**Degeneracy of S-matrices for conventional gradient metasurfaces and non-local metagratings.** Although gradient metasurfaces have been utilized to approach the second-order EP<sup>30</sup>, it is not trivial to extend this concept to a higher-order EP, since gradient metasurfaces lack the precise and effective control over the multiple propagating modes in a higher-order S-matrix. In order to clearly show whether the eigenvalues of the higher-order S-matrix of a gradient metasurface could collapse, we first investigate a 3-channel metasurface consisting of six grooves, with a period  $D = \sqrt{2}\lambda$ , by randomly assigning imaginary parts of the speed of sound  $\{c_n^i\}$  ( $n = 1, 2, \dots, 6$ ) to the six grooves. The real part of the speed of sound  $\{c_n^r\}$  follows the standard design procedure for gradient metasurfaces governed by the generalized law of reflection<sup>30</sup>. To ensure sufficient sampling to fully populate the parameter space, we randomly generate 100,000 sets of  $\{c_n^i\}$ , which represents the imaginary part of the normalized sound velocity and has the lower and upper bounds of 0 and 1. For each set of randomly assigned  $\{c_n^i\}$ , the differences between each two eigenvalues of the corresponding S-matrix are plotted in Fig. 2a-c. Here the x- and y-axes are the real and imaginary parts of the difference of the eigenvalues. A second-order EP can be manifested by data points covering the origin in any of the three figures, while a third-order EP requires that the data points cover the origins in all three figures. For this traditional gradient metasurface, a large blank area around the origin is found in Fig. 2a, b, while only the 2nd and 3rd eigenvalues may collapse (Fig. 2c), indicating a second-order EP. Therefore, a traditional metasurface is not an ideal candidate for accessing higher-order

EPs. The detailed geometrical parameters of the gradient metasurface and, among these samples, the behavior of a metasurface approaching a second-order EP can be found in Supplementary Note 2.

We then investigate a metagrating that also comprises six grooves periodically arranged as shown in Fig. 1. As opposed to conventional metasurfaces that are designed based on a local phase gradient, the metagrating here harnesses the interaction between the constituent grooves. In order to show that the non-local effect between sub-units are vital for the degeneracy of multiple eigenvalues, we again generate 100,000 non-local metagrating samples with randomly assigned imaginary parts of the speed of sound  $\{c_n^i\}$  ( $n = 1, 2, \dots, 6$ ), while their real parts  $\{c_n^r\}$ , relaxed from a gradient feature, now follows a particular distribution determined by the depths of the six grooves shown in Fig. 1. The results are shown in Fig. 2d-f. The data points are seen to spread more uniformly and in particular, those data points appear to cover the origins in all three figures, indicating the high probability of finding a third-order EP in such a scattering platform.

The results presented in Fig. 2 are generated using the coupled-mode theory, which takes non-local effects into account. To confirm the probability and exactly pinpoint the third-order EP, a global optimization algorithm is utilized (see details about the design procedure and parameters of the metagrating in Supplementary Note 3). Note that, to induce non-Hermiticity, the metagrating is assumed to have three grooves that are lossy in one period. The lossy grooves possess complex effective sound speeds, whose imaginary parts can be conveniently tuned by sound absorbing materials of the appropriate thickness.

**Behaviors of the non-local metagrating around the higher-order EP.** As an example, Fig. 3a shows the trajectories of the theoretically calculated eigenvalues as a function of the loss factor of the second groove,  $c_2^i$  (normalized imaginary part of the sound velocity), while those of the fourth and sixth grooves,  $c_4^i$  and  $c_6^i$ , are 0.053 and 0.601, respectively. As can be seen here, when  $c_2^i$  reaches 0.091, the trajectories of the three eigenvalues meet at a crossing point that is a direct manifestation precondition of the third-order EP.

Figure 3b-d shows the amplitudes of the wave that is retro-reflected through the left, normal and right channels, respectively. The three channels respond very differently to the same varying

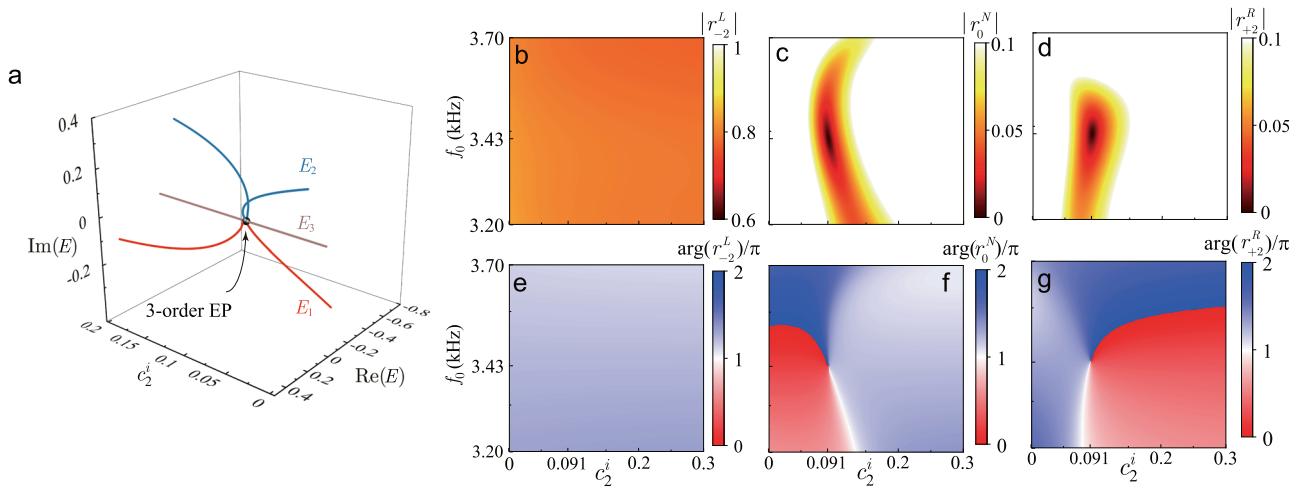


**Fig. 3 Eigenvalue and reflection coefficient distribution near the third-order exceptional point (EP).** **a** Variation of trajectories of the eigenvalues as functions of  $c_2^i$  (normalized imaginary part of the sound speed in the second groove).  $E_1$ ,  $E_2$  and  $E_3$  represent the three theoretically calculated eigenvalues, with the corresponding curves marked by different colors. The gray globe in the center represents the third-order EP. Calculated amplitude of retro-reflection coefficients,  $r_{-2}^L, r_0^N, r_{+2}^R$ , as functions of  $f_0$  (working frequency) and  $c_2^i$  in the left (**b**), normal (**c**) and right (**d**) channels, respectively.  $|r_0^N|, |r_{+2}^R| \geq 0.1$  inside the white regions in **c** and **d**. **e-g** Phases of the retro-reflection coefficients around the EP with the variation of  $f_0$  and  $c_2^i$ .

loss. While the left channel retro-reflection remains stable (a high efficiency around 0.81 for the reflection coefficient), the normal and the right channels are highly sensitive to even small variations of the loss factor. As can be seen, the system reaches the third-order EP, when  $c_2^i = 0.091$  and  $f_0 = 3430$  Hz, and as a result, the retro-reflections to the right and normal channels vanish, while the one to the left channel still remains strong. Furthermore, the vanishing channels experience a peculiar increase in amplitude beyond the EP, despite the very high loss factor in these regions of parameter space. This peculiar phenomena is known as loss enhanced reflection<sup>30</sup>. The phase variations shown in Fig. 3e-g also demonstrate the distinct behavior that corresponds to the occurrence of the third-order EP: a virtually constant phase shift throughout, for the left channel, but a trip point together with an abrupt phase shift at the EP for the normal and right channels. Furthermore, the amplitude and phase profiles are very much identical to those of the other diagonal coefficients ( $r_0^L, r_0^R$ ), as well as  $r_{+1}^R$  and  $r_{-1}^N$  (Supplementary Note 4).

**Enhanced sensitivity around the higher-order EP.** The strong parameter dependence observed above can be of great importance for detectors that require high sensitivity. Prior studies<sup>6</sup> have shown that the sensitivity,  $\Delta E$ , of a non-Hermitian system would increase with the order of the EP, as  $\Delta E \propto \delta^{1/N}$ , where  $\Delta E$  is the difference between real parts of the two eigenvalues and  $\delta$  represents the external perturbation. To corroborate this trend in the case of non-local metagratings, a two-channel metagrating that features a second-order EP is designed as shown in Supplementary Note 5, and its sensitivity is compared with that of the third-order metagrating discussed here. The external perturbation is induced in the lossy subunit as a disturbance in  $c_2^i$ , as  $c_2^i = c_2^i|_{EP} + \delta$ , where  $c_2^i|_{EP} = 0.091$ . The green stars in Fig. 4 show results from the analytical model and the curve-fitted solid red line illustrates that the sensitivity of the designed 3-channel metagrating follows a cube-root dependence on the induced perturbation ( $\Delta \propto \delta^{1/3}$ ). The second-order grating on the other hand has  $\Delta \propto \delta^{1/2}$ , as shown in Supplementary Fig. 6 in Supplementary Note 5.

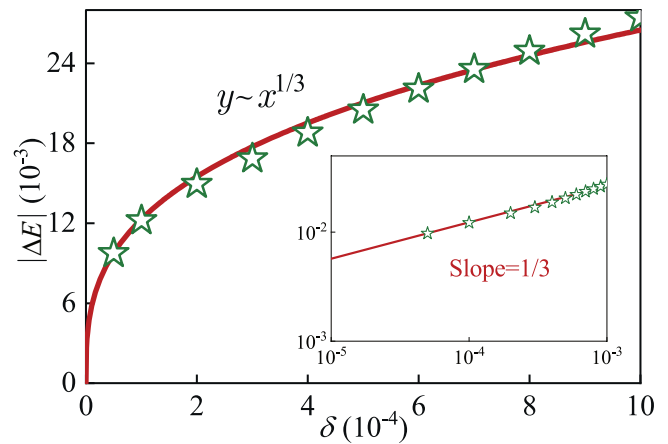


**Fig. 4 Sensitivity of the designed metagrating at the third-order exceptional point (EP).**  $\Delta E$  on the y-axis represents the difference between real parts of the first and second eigenvalues varying with the external perturbation  $\delta$ , i.e., disturbances in  $c_2^i$  (normalized imaginary part of the sound speed in the second groove). The green stars represent the difference calculated by the coupled mode theory. Red solid line shows corresponding fitting curves. The inset confirms the variation trajectory in the logarithmic scale.

**Experimental demonstration of the non-local metagrating at the higher-order EP.** The proposed metagrating is then experimentally verified via a sample of length 1.42 m (10 periods) that was placed in a two-dimensional waveguide of height 4 cm, where a 0.62 m line array with 17 speakers was used as the source. Figure 5a shows the constitution of experimental platform. Metagrating prototype is presented in the inset. To scan the field, a microphone moved with a step size of 0.01 m over the regions ( $0.4 \times 0.2$  m<sup>2</sup>) that correspond to the three channels, marked by the red dotted lines in Fig. 5b-d. They show the results from numerical simulations, in comparison to the measured results (normalized by the incident pressure) and indicates good agreement in Fig. 5e-g. Importantly, the strongly asymmetrical wave behavior is observable in experiments. When the left channel is

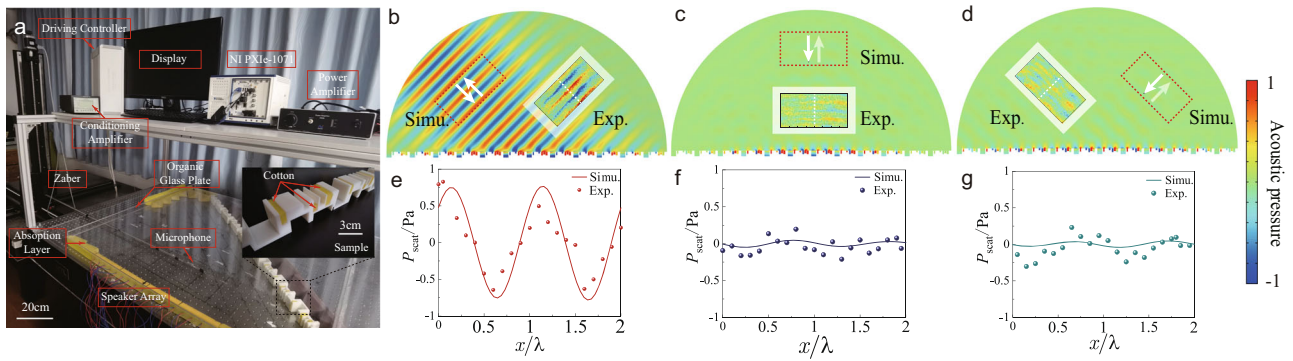


**Fig. 5 Experimental demonstration of the third-order exceptional point (EP).** **a** Experimental platform and the metagrating sample attached with melamine cotton. Simulated and experimental results (reflected field) of the multi-channel metagrating at the third-order EP under left (**b**), normal (**c**), and right (**d**) incidences. In each case, the scanning region is marked by a dotted-line box in the simulated wave field. The propagating waves are represented by white arrows while the less-visible arrows indicate the suppressed retro-reflection waves. For comparison, the measured reflected fields are shown with white borders on the side. **e-g** The simulated (lines) and measured (dots) pressure distributions along the center line of the scan area, as presented with white dotted lines in the upper panel.  $\lambda$  is the wavelength of the working frequency.

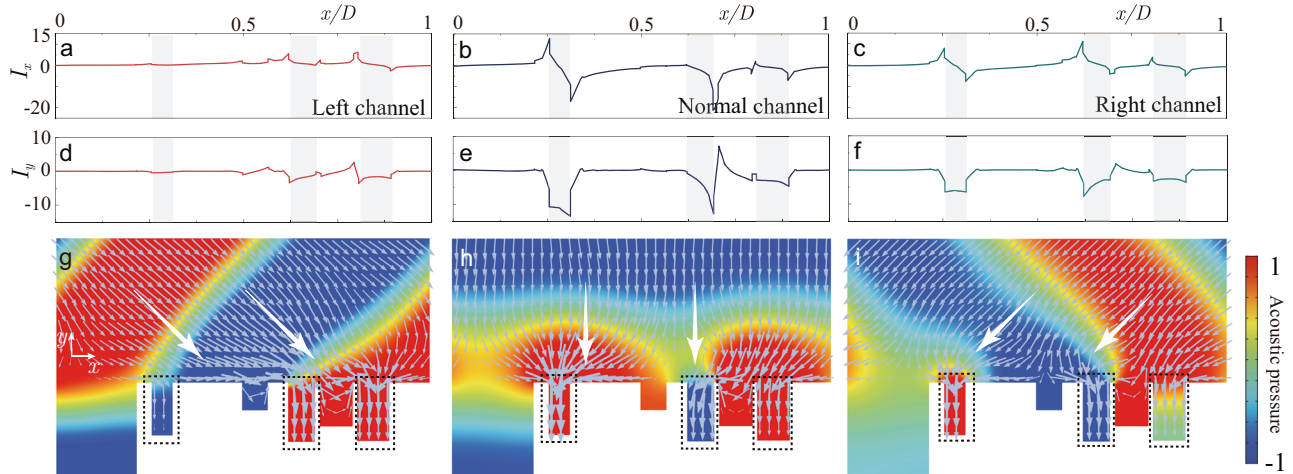


**Fig. 6 Non-local intensity flow distribution.** The  $x$ -components of the sound intensity (normalized by the incident field) along the metagrating surface under left (**a**), normal (**b**) and right (**c**) incidences.  $D$  is the period of the metagrating. The regions in gray identify the locations of lossy grooves. **d-f** The  $y$ -components of the sound intensity along the metagrating surface. The sound field distributions near the surface of the metagrating under left (**g**), normal (**h**) and right (**i**) incidences, where the color maps illustrate the acoustic pressure distributions and the gray arrows represent the energy flow. Areas bounded by dotted lines represent the lossy grooves. The white large arrows indicate the direction of incidence.

excited, retro-reflection is clearly observable, and the estimated reflection coefficient reaches around 0.75 (from the simulation and measured data in the lower inset of Fig. 5b). When sound is incident on the normal and right channels, however, the retro-reflection is strongly suppressed (Fig. 5c, d). Details of the experimental setup and the metagrating sample can be found in Method in reference.

**Energy exchange along the surface of the non-local metagrating.**

To shed light on the mechanism that gives rise to the asymmetric behavior in this non-local non-Hermitian metagrating, the local intensity distribution of the sound field is numerically calculated. Figure 6a-c shows the local acoustic intensity in the  $x$ -direction ( $I_x = \frac{1}{2} \text{Re}[p \times (v_x)^*]$ ), i.e., the product of pressure and complex conjugate of the local velocity in the  $x$ -direction) at the surface of metagrating for the cases of left, normal, and right incidence cases, respectively. Here, the “lossy” sites (three grooves with absorbing layers) are denoted by the regions in gray. It can be observed that  $I_x$  changes abruptly at the boundaries of these “lossy” regions, manifesting a strong nonlocality-induced lateral energy exchange with the neighboring grooves. Figure 6d-f shows

the intensity in the  $y$ -direction ( $I_y = \frac{1}{2} \text{Re}[p \times (v_y)^*]$ ), and illustrate that  $I_y$  is negative in the lossy regions due to absorption. It can be noted that the intensity here, fluctuates only slightly for the left incidence case (Fig. 6a, d) and suggests that the lossy grooves respond weakly and therefore renders a stable, highly efficient retro-reflection. This is in accordance with what is observed in Fig. 3b. Figure 6g-i shows the energy flow fields, where celadon arrows in the figures indicate the direction of the local intensity, and the length of arrows represent the intensity amplitude. The directions of the arrows are strongly distorted in the area very close to the surface, in sharp contrast to those in the far field. This unveils the fact that the designed metagrating utilizes the evanescent fields as a mechanism for channeling the energy along the surface of its sub-units.

**Conclusion**

To conclude, we have theoretically and experimentally investigated a non-local acoustic metagrating to illustrate the asymmetrical wave behavior that exists at the higher-order EP of its S-matrix. Since the general condition for engineering S-matrices with EPs of arbitrary orders is now established, more complicated

wave behavior can be envisioned (see the fourth-order EP shown in Supplementary Note 6). Our design suggests an efficient approach toward extremely asymmetric multi-channel wave manipulation with a high and controllable sensitivity and paves the way for acoustic impedance engineering via multi-functional anisotropic acoustic devices.

## Method

**Numerical simulations.** COMSOL Multiphysics and the frequency domain in acoustics in it are used here for the full-wave simulations. Density and velocity of air are set with  $\rho_0 = 1.28 \text{ kg m}^{-3}$  and  $c_0 = 343 \text{ m s}^{-1}$ , respectively. In Fig. 5b–d, scattering distribution is extracted from the semicircular sound field. The perfectly matched layers are used around them to reduce the edge reflections. Total field simulation around surfaces are shown in Fig. 6g–i. Floquet periodic conditions are applied into the left and right boundaries.

**Details of the experimental setup and the metagrating sample.** The top of the two-dimensional waveguide is an organic glass plate, which covers the sample in the experiment. The height of the waveguide is 4 cm to guarantee only the fundamental mode existing in  $y$ -direction in Fig. 1. The waveguide is surrounded by wedge cotton to allow waves to propagate out from the domain without reflection. The waveguide works in the range from 3 to 4.3 kHz. The sample of the metagrating was fabricated with stereo lithography apparatus, fed with sound waves generated by 17 one-inch loudspeakers, which can be controlled by the power amplifier (Brüel & Kjær Type 2734) at 3420 Hz. The 10 Hz difference in frequency between the theory and experiments could be explained by that sound speed in the lab environment is not in complete agreement with theory, i.e., 343 m/s. Signals of acoustic pressure and phase are collected by a 1/8-inch microphone (Brüel & Kjær Type 2670), which are then send to the data-acquisition hardware (NI PXI-4461 in NI PXIe-1071). In the experiment, the sound field was scanned twice, with and without the presence of sample. Then the reflected field from the metagrating can be obtained by subtracting the incident field (without the sample) from the total field (with the sample).

For the designed metagrating, loss is induced into three grooves, whose imaginary parts of the effective sound velocity are  $c_2^i = 0.091$ ,  $c_4^i = 0.053$ , and  $c_6^i = 0.601$ , respectively. In the experiment, it can be realized by tuning the thickness of the bottom absorbing layers (made of melamine cotton) in these grooves. The cross-section of the filling cotton is in consistent with the respective grooves. Here we numerically scanned the thickness of each packed cotton layer and calculated scattering field based on the Johnson-Champoux-Allard model (a poroacoustics model) from the Melamine cotton manufacturer. Then we found the corresponding cotton thickness that renders the groove reaching the same scattering field predicted by the prescribed  $c^i$ . Following this, now the 2nd, 4th and 6th grooves are filled with cotton with a ratio of 90%, 60%, and 100%, respectively. We note the limited accuracy in the cotton thickness may be one of the major factors that leads to the small deviation between the numerical prediction and the experimental results shown in Fig. 5b–g.

## Data availability

All data supporting the conclusions in the paper are present in the Supplementary Materials. Additional data that support the findings of this study are available from the corresponding author upon reasonable request.

Received: 30 July 2021; Accepted: 3 December 2021;

Published online: 20 December 2021

## References

- Bender, C. M. & Boettcher, S. Real spectra in non-hermitian hamiltonians having pt symmetry. *Phys. Rev. Lett.* **80**, 5243–5246 (1998).
- Dembowski, C. et al. Experimental observation of the topological structure of exceptional points. *Phys. Rev. Lett.* **86**, 787–790 (2001).
- Heiss, W. D. Exceptional points of non-hermitian operators. *J. Phys. A-Math. Theor.* **37**, 2455–2464 (2004).
- Moiseyev, N. *Non-Hermitian Quantum Mechanics* (Cambridge University Press, 2011).
- Peng, B. et al. Parity-time-symmetric whispering-gallery microcavities. *Nat. Phys.* **10**, 394–398 (2014).
- Hodaie, H. et al. Enhanced sensitivity at higher-order exceptional points. *Nature* **548**, 187–191 (2017).
- Miri, M. A. & Alu, A. Exceptional points in optics and photonics. *Science* **363**, 42–53 (2019).
- Feng, L., Wong, Z. J., Ma, R. M., Wang, Y. & Zhang, X. Single-mode laser by parity-time symmetry breaking. *Science* **346**, 972–975 (2014).
- Feng, L. et al. Demonstration of a large-scale optical exceptional point structure. *Opt. Exp.* **22**, 1760–1767 (2014).
- Zhang, X., Ding, K., Zhou, X., Xu, J. & Jin, D. Experimental observation of an exceptional surface in synthetic dimensions with magnon polaritons. *Phys. Rev. Lett.* **123**, 237202 (2019).
- Huang, Y., Veronis, G. & Min, C. J. Unidirectional reflectionless propagation in plasmonic waveguide-cavity systems at exceptional points. *Opt. Exp.* **23**, 29882–29895 (2015).
- Lin, Z. et al. Unidirectional invisibility induced by pt-symmetric periodic structures. *Phys. Rev. Lett.* **106**, 213901 (2011).
- Zhu, X. F., Ramezani, H., Shi, C. Z., Zhu, J. & Zhang, X.  $\mathcal{PT}$ -symmetric acoustics. *Phys. Rev. X* **4**, 031042 (2014).
- Ding, K., Ma, G. C., Xiao, M., Zhang, Z. Q. & Chan, C. T. Emergence, coalescence, and topological properties of multiple exceptional points and their experimental realization. *Phys. Rev. X* **6**, 021007 (2016).
- Liu, T., Zhu, X. F., Chen, F., Liang, S. J. & Zhu, J. Unidirectional wave vector manipulation in two-dimensional space with an all passive acoustic parity-time-symmetric metamaterials crystal. *Phys. Rev. Lett.* **120**, 124502 (2018).
- Achillesos, V., Theocharis, G., Richoux, O. & Pagneux, V. Non-hermitian acoustic metamaterials: role of exceptional points in sound absorption. *Phys. Rev. B* **95**, 144303 (2017).
- Zhang, J. et al. A phonon laser operating at an exceptional point. *Nat. Photon.* **12**, 479–484 (2018).
- Chen, W. J., Ozdemir, S. K., Zhao, G. M., Wiersig, J. & Yang, L. Exceptional points enhance sensing in an optical microcavity. *Nature* **548**, 192–196 (2017).
- Wang, H. M., Lai, Y. H., Yuan, Z. Q., Suh, M. G. & Vahala, K. Petermann-factor sensitivity limit near an exceptional point in a brillouin ring laser gyroscope. *Nat. Commun.* **11**, 1610 (2020).
- Djorve, P., Pennec, Y. & Djafari-Rouhani, B. Exceptional point enhances sensitivity of optomechanical mass sensors. *Phys. Rev. Applied* **12**, 024002 (2019).
- Wu, Y. L., Zhou, P. J., Li, T., Wan, W. S. & Zou, Y. High-order exceptional point based optical sensor. *Opt. Exp.* **29**, 6080–6091 (2021).
- Zhou, X. P. et al. Optical lattices with higher-order exceptional points by non-hermitian coupling. *Appl. Phys. Lett.* **113**, 101108 (2018).
- Li, Y., Liang, B., Gu, Z. M., Zou, X. Y. & Cheng, J. C. Reflected wavefront manipulation based on ultrathin planar acoustic metasurfaces. *Sci. Rep.* **3**, 2546 (2013).
- Xie, Y. et al. Wavefront modulation and subwavelength diffractive acoustics with an acoustic metasurface. *Nat. Commun.* **5**, 5553 (2014).
- Zhu, X. F. et al. Implementation of dispersion-free slow acoustic wave propagation and phase engineering with helical-structured metamaterials. *Nat. Commun.* **7**, 11731 (2016).
- Assouar, B. et al. Acoustic metasurfaces. *Nat. Rev. Mat.* **3**, 460–472 (2018).
- Zhu, Y., Gerard, N. J., Xia, X., Stevenson, G. C. & Assouar, B. Systematic design and experimental demonstration of transmission-type multiplexed acoustic meta-holograms. *Adv. Funct. Mater.* **31**, 2101947 (2021).
- Zhou, Z., Huang, S., Li, D., Zhu, J. & Li, Y. Broadband impedance modulation via non-local acoustic metamaterials. *Natl. Sci. Rev.* <https://doi.org/10.1093/nsr/nwab171> (2021).
- Li, Y. et al. Tunable asymmetric transmission via lossy acoustic metasurfaces. *Phys. Rev. Lett.* **119**, 035501 (2017).
- Wang, X., Fang, X. S., Mao, D. X., Jing, Y. & Li, Y. Extremely asymmetrical acoustic metasurface mirror at the exceptional point. *Phys. Rev. Lett.* **123**, 214302 (2019).
- Gerard, N. J. R. K. & Jing, Y. Loss in acoustic metasurfaces: a blessing in disguise. *MRS Commun.* **10**, 32–41 (2020).
- Song, A. L. et al. Asymmetric absorption in acoustic metamirror based on surface impedance engineering. *Phys. Rev. Applied* **12**, 054048 (2019).
- Yang, Y. Z., Jia, H., Bi, Y. F., Zhao, H. & Yang, J. Experimental demonstration of an acoustic asymmetric diffraction grating based on passive parity-time-symmetric medium. *Phys. Rev. Applied* **12**, 034040 (2019).
- Ra'di, Y., Sounas, D. L. & Alu, A. Metagratings: beyond the limits of graded metasurfaces for wave front control. *Phys. Rev. Lett.* **119**, 067404 (2017).
- Quan, L. & Alu, A. Hyperbolic sound propagation over nonlocal acoustic metasurfaces. *Phys. Rev. Lett.* **123**, 244303 (2019).
- Overvig, A. C., Malek, S. C. & Yu, N. Multifunctional nonlocal metasurfaces. *Phys. Rev. Lett.* **125**, 017402 (2020).
- Torrent, D. Acoustic anomalous reflectors based on diffraction grating engineering. *Phys. Rev. B* **98**, 060101 (2018).

## Acknowledgements

This work was supported by the National Key R&D Program of China (Grant Nos 2020YFA0211402), the National Natural Science Foundation of China (Grant Nos. 12074286, 11774265 and 12074288), and the Shanghai Science and Technology Committee (Grant Nos. 21JC1405600, 20ZR1460900, 20ZR1461700, and 20DZ1207200). N.J.R.K.G., Y.D., and Y.J. would like to thank NSF for the support through CMMI 1951221.

## Author contributions

Y.L. conceived the idea; X.F., N.J.G., and Y.D. carried out the theoretical analysis; X.F. designed the experiment; X.F., H.D., N.W., and B.J. performed the experiment and

analyzed data; X.W., Y.J., and Y.L. supervised the research; and X.F., Z.Z., N.J.G., Y.D., and X.W. wrote the paper with contribution from all authors.

### Competing interests

The authors declare no competing interests.

### Additional information

**Supplementary information** The online version contains supplementary material available at <https://doi.org/10.1038/s42005-021-00779-x>.

**Correspondence** and requests for materials should be addressed to Xu Wang, Yun Jing or Yong Li.

**Peer review information** *Communications Physics* thanks Chen Shen, Kunal Shastri and Pei Miao for their contribution to the peer review of this work. Peer reviewer reports are available.

**Reprints and permission information** is available at <http://www.nature.com/reprints>

**Publisher's note** Springer Nature remains neutral with regard to jurisdictional claims in published maps and institutional affiliations.



**Open Access** This article is licensed under a Creative Commons Attribution 4.0 International License, which permits use, sharing, adaptation, distribution and reproduction in any medium or format, as long as you give appropriate credit to the original author(s) and the source, provide a link to the Creative Commons license, and indicate if changes were made. The images or other third party material in this article are included in the article's Creative Commons license, unless indicated otherwise in a credit line to the material. If material is not included in the article's Creative Commons license and your intended use is not permitted by statutory regulation or exceeds the permitted use, you will need to obtain permission directly from the copyright holder. To view a copy of this license, visit <http://creativecommons.org/licenses/by/4.0/>.

© The Author(s) 2021